Biphoton state reconstruction via phase retrieval methods

NAZANIN DEHGHAN,[1,2] ⓘ ALESSIO D'ERRICO,[1,2,*] ⓘ FRANCESCO DI COLANDREA,[1] ⓘ
AND EBRAHIM KARIMI[1,2] ⓘ

[1]*Nexus for Quantum Technologies, University of Ottawa, Ottawa, Ontario K1N 6N5, Canada*
[2]*National Research Council of Canada, 100 Sussex Drive, Ottawa, Ontario K1A 0R6, Canada*
*aderrico@uottawa.ca

The complete measurement of the quantum state of two correlated photons requires reconstructing the amplitude and phase of the biphoton wavefunction. We show how, by means of spatially resolved single photon detection, one can infer the spatial structure of biphotons generated by spontaneous parametric down conversion. In particular, a spatially resolved analysis of the second-order correlations allows us to isolate the moduli of the pump and phase-matching contributions to the two-photon states. When carrying this analysis on different propagation planes, the free-space propagation of pump and phase-matching is observed. This result allows us, in principle, to gain enough information to also reconstruct the phase of the pump and the phase-matching and thus the full biphoton wavefunction. We show this in different examples where the pump is shaped as a superposition of orbital angular momentum modes or as a smooth amplitude with a phase structure with no singularities. The corresponding phase structure is retrieved employing maximum likelihood or genetic algorithms. These findings have potential applications in fast, efficient quantum state characterization that does not require phase locking of the unknown source with a reference biphoton. © 2024

1. INTRODUCTION

The tomography of quantum states plays a fundamental role in modern quantum technologies [1–5]. At the same time, such a task can be particularly challenging when dealing with systems of many particles and/or many degrees of freedom [6,7]. If a projective measurement approach is adopted, with no prior information, the number of required measurements scales quadratically with the dimensionality of the Hilbert space [1]. The case of the reconstruction of high-dimensional two-photon states is of particular interest given their applications in fundamental quantum mechanics [8–11], high-dimensional quantum communications [12,13], and quantum imaging [14]. As an alternative to projective approaches based on mode sorting, recent works introduced the possibility of exploiting variations of classical interferometric techniques for directly reconstructing the spatial structure of phase and amplitude of an unknown biphoton state [15]. This approach is practically faster and more reliable than traditional methods thanks to the use of time-stamping cameras [16–18], which is proving to be a promising resource for quantum optics experiments [15,19–27]. However, interferometric approaches will require the phase locking of the reference biphoton state with the unknown one, a task which can be harder to achieve in cases where the unknown source is not easily accessible. It is thus desirable to have the possibility of obtaining the phase structure of the unknown biphoton from measurements that do not require any control of the source. Here,

we propose a method based on measuring the spatial coincidence distribution in different propagation planes and reconstructing the phase of the biphoton employing phase retrieval algorithms. Non-interferometric phase retrieval is emerging as an interesting tool in quantum imaging applications [27,28].

We demonstrate how the analysis of coincidence images allows us to extract the square moduli, hereafter referred to as "intensities," of the two complex functions that contribute to the biphoton state: the pump and the phase-matching. Intriguingly, in the case of free-space propagation, this separation can be performed in any plane perpendicular to the average propagation direction, here identified with the z axis. The intensity of the extracted pump (phase-matching) function in a given plane $z = z_0 + d$ is related to the pump (phase-matching) in $z = z_0$ by paraxial propagation through a distance $d/2$—or, equivalently, assuming the pump and phase-matching functions to have half the wavelength of the biphoton state. Retrieving pump and phase-matching intensities at different planes and knowing their relationship opens the possibility of reconstructing the phase of these fields and, thus, the full biphoton wavefunction. We show, theoretically and experimentally, how to isolate the pump and phase-matching intensities from coincidence images. Therefore, we give some examples of their phase reconstruction based on the exploitation of maximum likelihood approaches and genetic algorithms. The latter are used in cases where the convenient modal decomposition—e.g., Zernike polynomial expansion of the pump

phase—does not have an analytical expression for the field propagation. Last, we give an example of a more complex situation where a sharp image is encoded in the pump's phase.

2. THEORY

Consider a two-photon state with fixed wavelengths and polarizations, in a paraxial propagation regime. In this case, assuming the z axis corresponds to the mean propagation direction, the system can be described in terms of the probabilities of photons passing through the transverse position $\mathbf{X} = (x, y)$ in a given plane. The quantum state is thus described in terms of the creation operators $\hat{a}_{\mathbf{X}}^{\dagger}$. Defining the transverse position eigenstate as $|\mathbf{X}\rangle := \hat{a}_{\mathbf{X}}^{\dagger}|0\rangle$, with $|0\rangle$ the vacuum state, a general biphoton state is given by

$$|\Psi\rangle = \iint \Psi(\mathbf{X}_i, \mathbf{X}_s)|\mathbf{X}_i\rangle \otimes |\mathbf{X_s}\rangle \mathrm{d}\mathbf{X}_i \mathrm{d}\mathbf{X}_s, \tag{1}$$

where $\Psi(\mathbf{X}_i, \mathbf{X}_s)$ is called the biphoton wavefunction. The indices i and s denote, conventionally, *idler* and *signal* photons, respectively. Equation (1) is a representation of the state in a basis of transverse coordinates eigenstates for a given value of z. The free-space propagation of the biphoton wavefunction from z to z' is

$$\Psi'(\mathbf{X}_i', \mathbf{X}_s') = \iint \mathcal{G}_{\Delta z}(\mathbf{X}_i', \mathbf{X}_i)\mathcal{G}_{\Delta z}(\mathbf{X}_s', \mathbf{X}_s)$$

$$\times \Psi(\mathbf{X}_i, \mathbf{X}_s)\mathrm{d}\mathbf{X}_i \mathrm{d}\mathbf{X}_s, \tag{2}$$

where $\mathcal{G}_{\Delta z}(\mathbf{X}', \mathbf{X})$ is a free-space propagator through the distance $\Delta z = z' - z$ and $\mathbf{X}' = (x', y')$ are the transverse coordinates in the plane z'. For paraxial fields, the free-space propagation is described in terms of the Fresnel propagator

$$\mathcal{G}_z(\mathbf{X}', \mathbf{X}) = \frac{i}{\lambda z}e^{ikz}\exp\left(-i\frac{\pi}{\lambda z}(\mathbf{X}' - \mathbf{X})^2\right). \tag{3}$$

A common and interesting case is given by correlated biphoton states with the following wavefunction:

$$\Psi(\mathbf{X}_i, \mathbf{X}_s) = \mathcal{E}_p\left(\frac{\mathbf{X}_i + \mathbf{X}_s}{2}\right)\phi\left(\frac{\mathbf{X}_i - \mathbf{X}_s}{2}\right). \tag{4}$$

In particular, in the case of biphotons generated via spontaneous parametric down conversion (SPDC) in Type-I crystals, $\mathcal{E}_p$ is the spatial, slowly varying amplitude of the pump laser, and ϕ is the phase-matching function [29,30]. This structure simplifies the propagation of the biphoton wavefunction significantly. Performing the change of variables $\mathbf{R} = (\mathbf{X}_i + \mathbf{X}_s)/2$, $\boldsymbol{\Delta} = (\mathbf{X}_i - \mathbf{X}_s)/2$ [24], and expanding the squares $(\mathbf{X}' - \mathbf{X})^2$ in the Fresnel propagator, it is straightforward to verify that

$$\mathcal{G}_z(\mathbf{X}_i', \mathbf{X}_i)\mathcal{G}_z(\mathbf{X}_s', \mathbf{X}_s) = \frac{1}{4}e^{ikz}\mathcal{G}_{z/2}(\mathbf{R}', \mathbf{R})\mathcal{G}_{z/2}(\boldsymbol{\Delta}', \boldsymbol{\Delta}). \tag{5}$$

This allows one to separate the four-dimensional (4D) integral describing the SPDC propagation in free space into the product of two bidimensional integrals:

$$\Psi'(\mathbf{R}', \boldsymbol{\Delta}') = \mathcal{N}\int \mathcal{G}_{\Delta z/2}(\mathbf{R}', \mathbf{R})\mathcal{E}_p(\mathbf{R})\mathrm{d}\mathbf{R}$$

$$\times \int \mathcal{G}_{\Delta z/2}(\boldsymbol{\Delta}', \boldsymbol{\Delta})\phi(\boldsymbol{\Delta})\mathrm{d}\boldsymbol{\Delta}, \tag{6}$$

where $\mathcal{N}$ is a normalization constant. Thus, the propagated biphoton wavefunction has the structure $\Psi'(\mathbf{R}', \boldsymbol{\Delta}') = \mathcal{E}_p'(\mathbf{R}')\phi'(\boldsymbol{\Delta}')$, where $\mathcal{E}_p'$ and ϕ' are obtained applying a single Fresnel propagator on the functions $\mathcal{E}_p$ and ϕ. It is important to emphasize that the propagation of $\mathcal{E}_p$ and ϕ must be evaluated for $\Delta z/2$ if Δz is the propagation distance considered for the biphoton state.

Experimentally, from spatially resolved coincidence detection, one can extract the pump and phase-matching contributions in each measurement plane. Coincidence detection with event based cameras allows us to retrieve the 4D function $\mathcal{C}(\mathbf{X}_i, \mathbf{X}_s) = |\Psi(\mathbf{X}_i, \mathbf{X}_s)|^2$. From $\mathcal{C}$ one can easily extract useful information expressed by 2D functions, such as the spatial correlations in the x and y coordinates, which are defined as the marginal distributions $\mathcal{C}_x(x_i, x_s) := \iint \mathrm{d}y_i \mathrm{d}y_s \mathcal{C}(\mathbf{X}_i, \mathbf{X}_s)$ and $\mathcal{C}_y(y_i, y_s) := \iint \mathrm{d}x_i \mathrm{d}x_s \mathcal{C}(\mathbf{X}_i, \mathbf{X}_s)$. An example of spatial correlations on SPDC in an intermediate propagation plane is shown in Figs. 1(a) and 1(b). Another quantity of interest is what we denote as a *coincidence image*, which is defined by integrating over one of the two photon's coordinates, e.g., $\mathcal{C}_s(x_s, y_s) := \iint \mathrm{d}x_i \mathrm{d}y_i \mathcal{C}(\mathbf{X}_i, \mathbf{X}_s)$. As can be seen in Fig. 1(c), the coincidence image shape depends on both the pump and phase-matching functions, displayed in Fig. 1(d) and 1(e), respectively. The latter can be extracted by applying filters on the coincidence distribution before integrating on the signal photon's coordinates. In particular, we consider *post-selected coincidence images* of the form

$$\mathcal{C}_{\pm}(\mathbf{X}_s) := \iint \mathrm{d}^2\mathbf{X}_i \mathcal{C}(\mathbf{X}_i, \mathbf{X}_s)\delta(\mathbf{X}_i \mp (\mathbf{X}_s - 2\mathbf{c})). \tag{7}$$
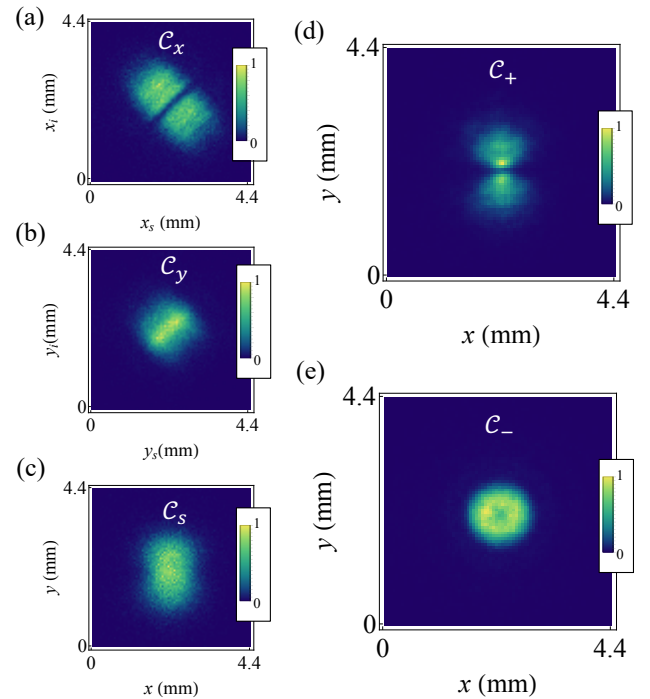

Fig. 1. 2D distributions extracted from the coincidences. Panels (a) and (b) show an example of spatial correlations obtained integrating a measured coincidence distribution along the y and x coordinates of signal and idler photon, respectively. (c) The coincidence distribution in the signal path is shown. The shape of this distribution depends both on the pump and phase-matching contributions. These can be isolated post-selecting on either correlations or anti-correlations, i.e., calculating (d) $\mathcal{C}_+$ and (e) $\mathcal{C}_-$, respectively.

From Eqs. (1) and (6), it is straightforward to see that, in any propagation plane, the post-selected coincidence images yield the pump and phase-matching squared moduli:

$$\mathcal{C}_+(\mathbf{X}_s, \mathbf{c}) = |\mathcal{E}_p(\mathbf{X}_s - \mathbf{c})|^2 |\phi(\mathbf{c})|^2, \qquad (8)$$

$$\mathcal{C}_-(\mathbf{X}_s, \mathbf{c}) = |\phi(-\mathbf{X}_s + \mathbf{c})|^2 |\mathcal{E}_p(\mathbf{c})|^2. \qquad (9)$$

Apart from a constant shift $\mathbf{c}$, the post-selected coincidences give patterns that are spatially distributed as the pump and the phase-matching intensity, respectively. Here, we considered a generic case in which correlations and anti-correlations are chosen with a constant offset $\mathbf{c}$. This allows for increasing the statistics without the need for long exposure times in the experiment—see the following section and Supplement 1, Fig. S1.

Since this result holds true for any z, we can extract the individual functions of the pump $\mathcal{E}_p(z)$ and phase-matching $\phi(z)$ that contribute to the biphoton state and observe how these functions propagate in free space. By examining the distributions of the pump and phase-matching functions in different planes, it is possible to obtain information on their phase structure without the need for interferometric or tomographic measurements.

3. EXPERIMENTAL RESULTS

We observed the free-space propagation of the pump and phase-matching contribution of an SPDC state generated in a 0.5 mm thick Type-I BBO crystal pumped by a pulsed 405 nm laser beam (pulse duration 150 fs, repetition rate 80 MHz). A liquid crystal spatial light modulator (LC-SLM) was used to shape the spatial structure of the pump laser. A conceptual scheme of the experiment is sketched in Fig. 2(a), while the detailed setup is described in Section 5. Idler and signal photons can be separated in two different paths—with 50% probability—by a non-polarizing beamsplitter and imaged on two regions of a time-stamping

camera (Timepix3D) [16,18,31]. If the spatial distributions of the idler and signal do not overlap on the camera sensor, one can choose two regions of interest (ROIs), defined as the groups of pixels hit by the idler and signal photons, respectively. The time-stamping resolution of the Timepix3D is less than 10 ns and allows us to extract coincidences between pixels contained in the ROIs, $\mathcal{C}(\mathbf{X}_i, \mathbf{X}_s)$. From the 4D coincidence distribution it is possible to extract marginals, e.g., the spatial correlations along x: $\mathcal{C}_x(x_i, x_s) = \sum_{y_i, y_s} \mathcal{C}(x_i, y_i, x_s, y_s)$. Alternatively, 2D sections of the 4D coincidence pattern can be extracted. As shown by Eqs. (8) and (9), this allows us to obtain the intensity distributions $|\mathcal{E}_p(\mathbf{X} - \mathbf{c})|^2$ and $|\phi(-\mathbf{X} + \mathbf{c})|^2$, where the constant $\mathbf{c}$ can be chosen at will. To fully exploit the accumulated data, one can sum up the intensities obtained for each value of $\mathbf{c}$ after appropriately shifting each distribution by $\pm\mathbf{c}$. Indeed, we have that $\sum_{\mathbf{c}} \mathcal{C}_+(\mathbf{X} + \mathbf{c}) = |\mathcal{E}_p(\mathbf{X})|^2 \sum_{\mathbf{c}} |\phi(\mathbf{c})|^2 = |\mathcal{E}_p(\mathbf{X})|^2$ and $\sum_{\mathbf{c}} \mathcal{C}_-(\mathbf{X} + \mathbf{c}) = |\phi(\mathbf{X})|^2 \sum_{\mathbf{c}} |\mathcal{E}_p(\mathbf{c})|^2 = |\phi(\mathbf{X})|^2$, where in the last equalities we assumed that $\mathcal{E}_p$ and ϕ are normalized to 1. In this way, it is possible to achieve smooth reconstructions from data obtained with a few minutes of exposure (see Supplement 1, Fig. S1, Visualization 1 and Visualization 2). A first example of the reconstruction is shown in Figs. 2(b) and 2(c) for the case of a Gaussian pump. The analysis was carried out in two different propagation planes at distances $z_1 = 7.5$ cm and $z_2 = 34.5$ cm from the image plane of the crystal. The spatial correlations show the evolution from a spatially correlated state (signal and idler photon are localized in roughly the same transverse position) to a spatially anti-correlated state (signal and idler photons are localized in opposite transverse positions with respect to the biphoton state propagation axis). The correlations do not appear particularly sharp in these two planes. However, their width is of the order of a single pixel in the crystal image plane (an example is shown in Supplement 1, Fig. S3). The extracted pump intensities display the expected Gaussian distribution (slightly narrower in z_2 due to a wavefront curvature of the pump laser on the crystal plane).
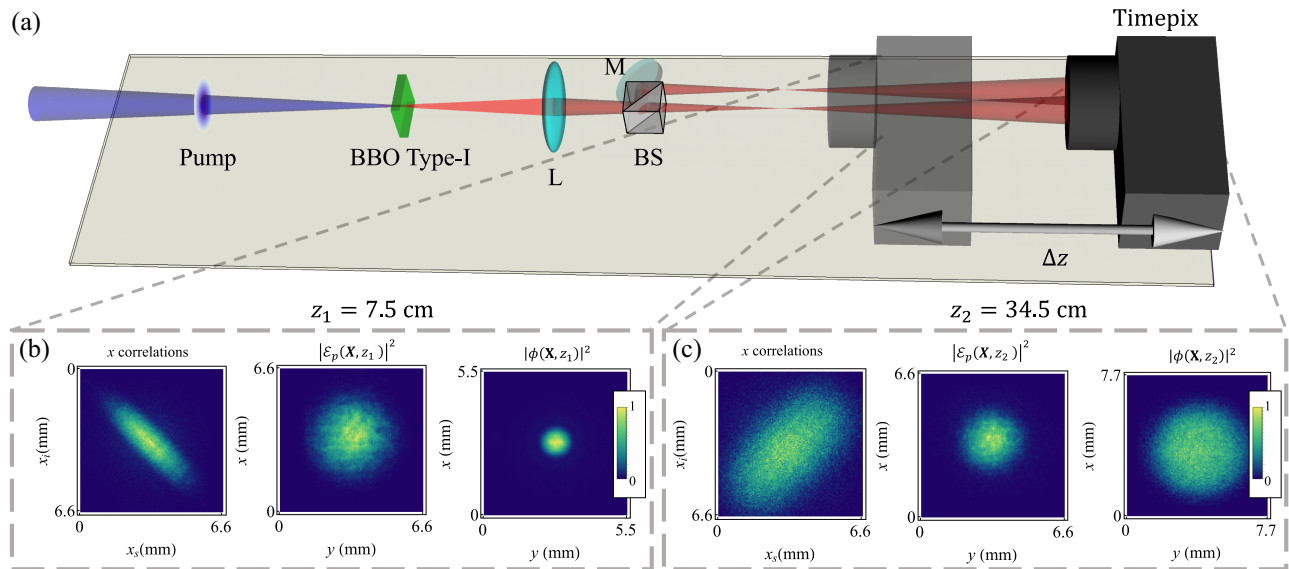

Fig. 2. Experimental layout and coincidence analysis. (a) Simplified sketch of the experimental setup. A pump laser (central wavelength 405 nm) is incident on a 0.5 mm thick BBO Type-I crystal that generates photon pairs with the same polarization. The photons propagate through an imaging system (depicted here as a single lens L; see Section 5 for the detailed experimental layout). Signal and idler photons are spatially separated with a 50/50 beamsplitter (BS) and impinge on a time-stamping camera (Timepix), which allows for retrieving spatially resolved coincidence counts. The camera was moved along the propagation direction to measure spatial correlations in different planes and extract the corresponding pump and phase-matching function intensities. An example with a Gaussian pump is shown in panels (b) and (c).

The extracted phase-matching intensity shows the formation of the characteristic SPDC cone in a collinear phase-matching configuration.

It is well known that measuring the intensity distribution of a coherent beam in two different propagation planes can be used to retrieve the phase. This non-interferometric phase retrieval approach was first proposed by Gerchberg and Saxton [32] for the case where the two intensity distributions are measured in conjugate planes (i.e., the corresponding fields are one the Fourier transform of the other). Unfortunately, doing this for an SPDC state implies that, for instance, the reconstructed phase-matching intensity will have a width of one or a few pixels in the first recording plane (and a similar effect will be observed for the pump distribution in the far field). This is due to the fact that the spatial extension of pump and phase-matching functions is extremely different on these two planes. One can then think of looking for a compromise and choose two intermediate planes sufficiently far away from each other but where the spatial extension of the pump and phase-matching are of the same order. However, in these cases, the Gerchberg–Saxton (GS)—as well as variations such as the Fienup algorithm [33,34]—tends to have a worse convergence and be sensitive to noise. This is acceptable for applications where a phase pattern is generated to achieve target intensities but is less practical for phase retrieval since the GS can easily converge to local minima characterized by strongly irregular phase patterns. We thus expect the GS approach to be useful only in cases of rather complex, rapidly diffracting pump fields, while for smoother and simple structures we focused on retrieving the phase structure of phase-matching and pump using optimization algorithms. However, these algorithms rely on some assumptions about the modal structure of the measured quantities. This is not a big issue since the SPDC physics for thin crystals has been extensively studied and SPDC spatial mode structures are expected to follow the field continuity.

As a first step, we consider the phase retrieval of the phase-matching function ϕ. In Figs. 3(a) and 3(b), we report the measured intensity $|\phi(\mathbf{X}, z)|^2$ in two different planes. $\phi(\mathbf{X}, z)$ propagates essentially as a strongly diverging beam. One can expect—as also predicted by the thin-crystal theory of SPDC—that the phase of ϕ in a given plane is quadratic: $\arg \phi(\mathbf{X}, z) = \pi \mathbf{X}^2/(\lambda z)$. When applying this phase structure on the amplitude measured in z_2 and numerically propagating back to z_1, one obtains the intensity displayed in Fig. 3(c), which is in good agreement with the experimental result. The reconstructed phase-matching function is shown in Fig. 3(c). The same phase structure was obtained via an optimization algorithm based on the decomposition of the phase-matching function in orthogonal modes. We describe this process for the reconstruction of the pump phase in detail below.

Pump lasers, prepared in spatial structures different from a single Gaussian, have been considered, e.g., to shape correlations in the orbital angular momentum (OAM) degree of freedom [7] or to control multimode Hong–Ou–Mandel bunching or antibunching [35]. In the latter case, one considers a pump field that is an asymmetric function of one transverse coordinate. This is obtained by applying a π-phase jump on an input Gaussian beam. Figure 4 a shows the pump intensity contribution to the SPDC state in two different propagation planes. To retrieve the phase structure of the corresponding field, we consider its approximation to a finite superposition of paraxial modes $f_\kappa(\mathbf{X}, z)$,
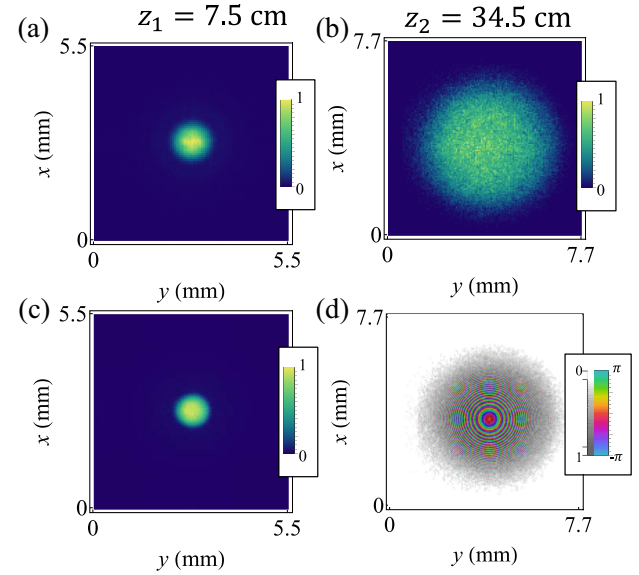

Fig. 3. Full reconstruction of phase-matching function. (a), (b) Experimentally extracted intensity of the phase-matching function of an SPDC state in two different propagation planes. (c) Reconstructed phase-matching intensity in z_1, obtained by assuming the quadratic phase shown in panel (d) and applied on the experimental amplitude in z_2. The intensity in z_1 is obtained by Fresnel propagation. The excellent agreement with the experimental intensity in z_1 indicates the correctness of the assumed phase structure. This agreement can be quantified by the similarity (see Supplement 1), which in this case is 94%.

$$\mathcal{E}_p(\mathbf{X}, z) \approx \sum_\kappa c_\kappa f_\kappa(\mathbf{X}, z). \tag{10}$$

Here, κ is, in general, a set of discrete indices. If the pump intensity in two different planes is $I_i(\mathbf{X}) = |\mathcal{E}_p(\mathbf{X}, z_i)|^2$, with $i = 1, 2$, then the optimal modal decomposition can be found minimizing the functional

$$\mathcal{L}[\{c_\kappa\}] := \iint \sum_i \left| I_i(\mathbf{X}) - |\sum_\kappa c_\kappa f_\kappa(\mathbf{X}, z_i)|^2 \right| \mathrm{d}^2 X. \tag{11}$$

The choice of the modes set and the range of values for κ varies case by case. Typical choices can be the Hermite–Gauss or Laguerre–Gauss sets [36]. However, spatially shaped beams are often generated by applying a phase pattern with line or point singularities on an input Gaussian beam. This typically requires a large number of coefficients in the decomposition Eq. (10). In this situation, another convenient choice is the over-complete set of hypergeometric-Gauss modes $\mathrm{HyGG}_{-|\ell|,\ell}(\mathbf{X})$ [37]—the detailed expression used in this work is given in Section 5. We recall that the index ℓ refers to the orbital angular momentum (in units of $\hbar$) carried by the corresponding mode. The coefficients c_ℓ will thus give the OAM spectrum of the analyzed field. Figure 4(b) shows the field intensity of the decomposition (10) obtained minimizing Eq. (11) where $f_\kappa \rightarrow \mathrm{HyGG}_{-|\ell|,\ell}$. The excellent agreement with the experimental data is also highlighted in Fig. 4(c), where the experimental amplitude distribution along y, for fixed $x = 1.9$ mm, is compared with the reconstructed one. Figure 4(c) shows the reconstructed field in $z = 0$. A phase variation of $\sim\pi$ between the two intensity maxima can be observed, together with an overall smooth quadratic phase due to the imperfect collimation of the pump on the crystal. In Fig. 4(e), the OAM
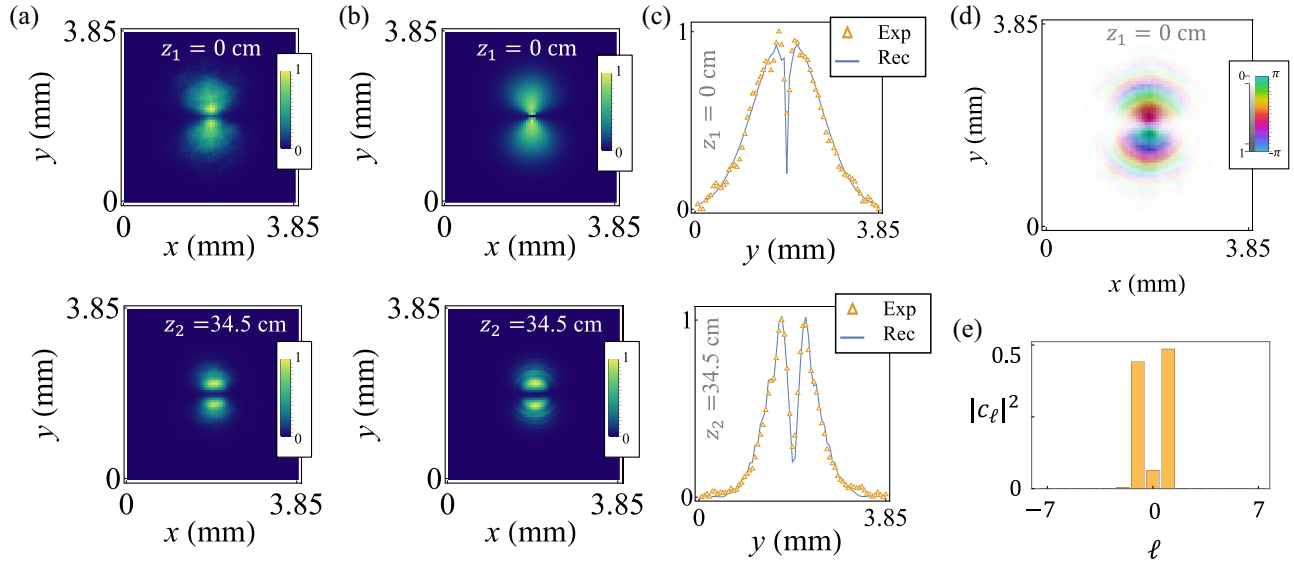
Fig. 4. Phase reconstruction of the anti-symmetric state. (a) Pump intensities for an anti-symmetric SPDC state are extracted by calculating $\mathcal{C}_+(\mathbf{X})$ from the experimental coincidences. (b), (c) Reconstructed intensities from an optimal superposition of HyGG modes that best matches the experimental data in panel (a). The similarities between reconstructed and measured intensity are 97% for the plane $z_1 = 0$ cm and 99% for $z_2 = 34.5$ cm. Panel (c) shows the comparison with the experiment (gold-colored triangles) along the line $x = 1.6$ mm. (d) Reconstructed phase and amplitude of the pump contribution in z_1. (e) Reconstructed OAM power spectrum, which does not change in propagation, of the pump field.

power spectrum is reported, showing how the main contribution comes from two OAM modes with $\ell = \pm 1$. The smaller $\ell = 0$ contribution (associated with a Gaussian mode) is due to a residual misalignment of the SLM phase mask. In Fig. 5, we consider a pump created in an unbalanced superposition of OAM modes, mainly with $\ell = -2$ and $\ell = 4$. This superposition exhibits a six-lobe intensity pattern, similarly to the one that could be encountered by an equal superposition of $\ell = 3$ and -3. The intensity of the latter, however, will propagate differently from the state here considered, and indeed the minimization algorithm converges to the correct solution. A finite decomposition in 15 HyGG modes (with $\ell = -7, \ldots, 7$) yields a reconstruction that matches well the experimental data. The OAM power spectrum is peaked at the expected OAM values. The small contributions around $\ell = 4$ and $\ell = -2$ are likely due to a small misalignment of the generation hologram.

The use of a finite set of orthogonal modes can be less efficient for fields with no phase singularities. In most applications, SPDC is generated by a pump in the fundamental mode of the laser cavity; however, the actual phase and amplitude can be altered by imperfections in the experimental setup. Thus, one can expect that the pump contribution has a smooth phase factor that can be expanded in Zernike polynomials. We provide proof of principle for these applications by introducing specific optical aberrations on the Gaussian pump with a UV-SLM. Figures 6(a)–6(d) show the extracted pump shapes in the crystal image plane $z_1 = 0$ and at $z_2 = 19$ cm for cases in which a coma and a second-order astigmatism phase were introduced on the pump. We assumed the phase $\xi_p(\mathbf{X}, z = 0)$ to be a superposition $\xi_p(\mathbf{X}, z = 0) = \sum_{n,m} \gamma_{n,m} Z_n^m(\mathbf{X})$, where $Z_n^m(\mathbf{X})$ are Zernike polynomials [38] and $\gamma_{n,m}$ are real coefficients, while the amplitude is given by the square root of the experimentally retrieved intensity. Due to the lack of analytical expression for the
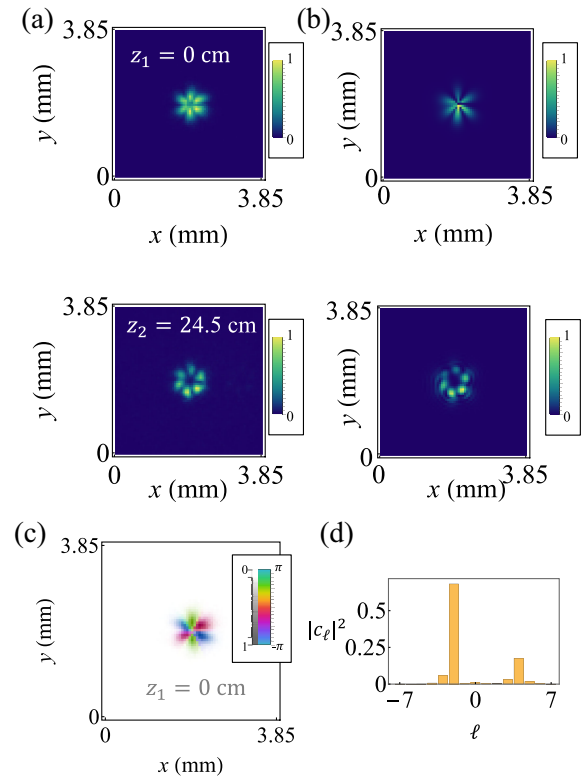

Fig. 5. Phase reconstruction of OAM superposition states. (a) Experimentally retrieved pump intensity in a superposition of, nominally, OAM = 4 and OAM = −2. (b) Intensities of the reconstructed field obtained by superimposing 15 HyGG modes. The agreement is confirmed by the similarity being 92% in z_1 and 89.6% in z_2. (c) Retrieved phase and amplitude of the pump contribution at the crystal image plane. (d) (Propagation-invariant) OAM power spectrum of the reconstructed field.
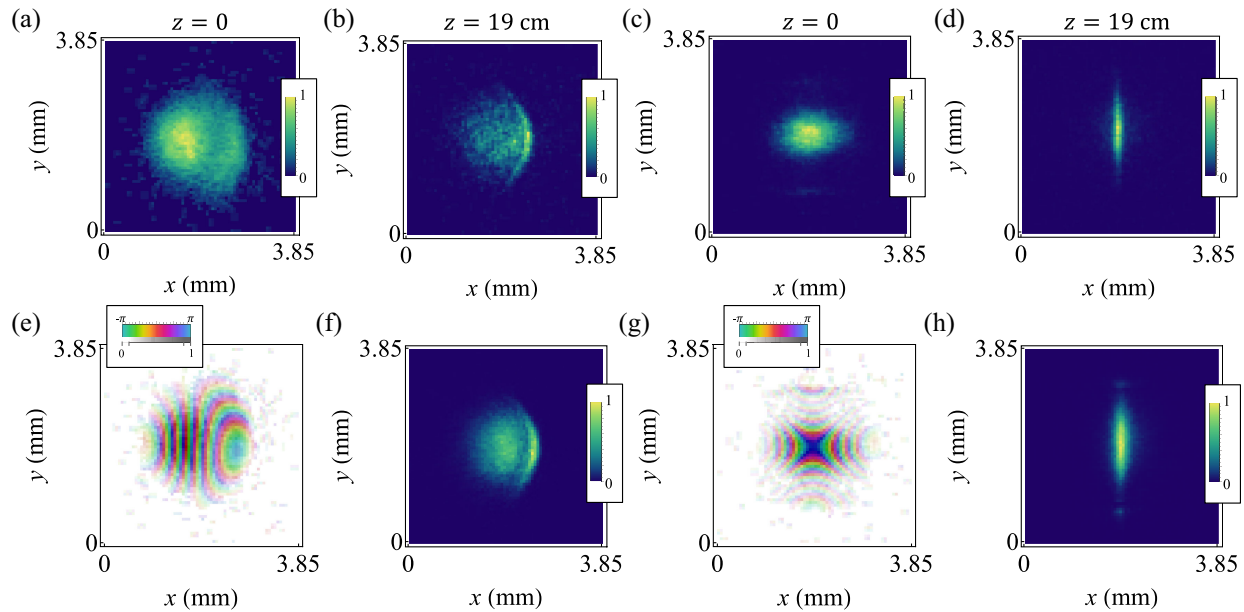
Fig. 6. Phase reconstruction of aberrated Gaussian pumps. Panels (a)–(d) show the extracted pump shapes in two propagation planes, $z = 0$ and 19 cm. For (a) and (b), a coma aberration was imposed through an SLM on the pump laser. For (c) and (d), instead, second-order astigmatism was applied on the pump laser. Panels (e) and (g) show the reconstructed phase and amplitude distributions in $z = 0$. In contrast, (f) and (h) show the intensity obtained by numerically propagating the fields in (e) and (g) to $z = 19$ cm [to be compared with panels (b) and (d), respectively]. Similarities are of the order of 90 % (see Supplement 1, Fig. S2). The phase distributions in (e) and (g) are shown with the tip and tilt contributions removed since these are due only to the imperfect centering of the intensity patterns in the two planes.

propagation of aberrated modes, we relied on the use of a genetic algorithm instead of the maximum likelihood approach used in the previous examples. Random choices of $\gamma_{n,m}$ were used to define the individuals that initialize the genetic algorithm. A numerical Fresnel propagation approach was used to calculate the fields in z_2 resulting from the different individuals and compare the intensity with the experimental one. The function in Eq. (11) was here used as the fitness function of the genetic algorithm (details are given in Section 5 and Supplement 1). Figures 6(f) and 6(h) show the best-reconstructed pump field at z_2—which is in good agreement with the experiment—and the corresponding amplitude and phase in z_1 are shown in Figs. 6(e) and 6(g).

The examples given thus far rely on the assumption of a limited decomposition in orthogonal modes of the field (or the phase in the last example). To explore the applicability of this method to more complex fields whose decomposition requires a much larger set of modes, we consider the case in which the pump consists of a Gaussian intensity with a phase image with sharp edges. The choice is motivated by the idea of extending this approach towards quantum phase imaging applications. Figures 7(a) and 7(b) show the results in the case the phase structure of the pump is a maple leaf with a phase difference between the interior and exterior part of π. The experimental data were used to feed a modified GS algorithm that exploits the Fresnel propagation instead of the Fourier transform. The reconstructed field is shown in Fig. 7(c). The expected phase jump is evident; however, the reconstruction quality seems to be affected by the low spatial resolution of the camera.

4. DISCUSSION AND CONCLUSIONS

In conclusion, we have shown a powerful application of coincidence imaging of biphoton states. Spatially resolved second-order correlations allow the extraction of information about the two main physical contributions to the SPDC biphoton states, the spatial structure of the pump beam and the phase-matching function, which is determined by the physical properties of the nonlinear crystal used for the biphoton state generation. The intensity of these two functions can be extracted at any distance from the crystal, and the relationship of the obtained intensities at different distances is given by an appropriate paraxial propagation. By employing optimization methods, we exploited these results to extract the phase of the two investigated functions and, thus, the full biphoton state. It must be stressed that this high-dimensional state reconstruction requires only two spatially resolved coincidence measurements, which, thanks to modern time-stamping cameras, can be performed in a few minutes without any control of the biphoton source. However, the renunciation of interferometric methods, and thus of direct phase measurements, comes at the expense of designing the proper algorithm to find the best phase structure that describes the experimental results. For smooth phases, if the field intensities are retrieved in propagation planes too close to each other, there will be a higher uncertainty in the reconstructed phase. Moreover, the separation of pump and phase-matching can be rigorously achieved when the transverse walk-off between pump and down-converted photons is negligible, e.g., for thin crystals or, in general, pump lasers collimated within the crystal thickness. The more general scenario will require more robust approaches to analyze the 4D second-order correlations in different propagation planes and extract the full phase patterns. We expect that this problem could be tackled by utilizing properly trained neural networks. Lastly, the ability to separate pump and phase-matching contributions opens new opportunities for quantum imaging applications, some of which will be explored in future works.
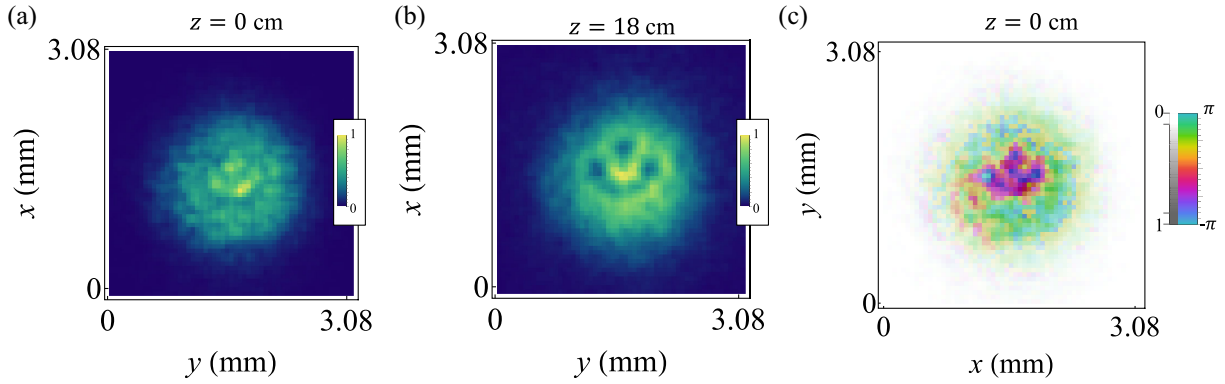
Fig. 7. Phase image encoded in Gaussian pumps. A phase structure consisting of a maple leaf pattern with a phase jump of π between the interior and the exterior part of the leaf was applied on the pump laser. The reconstructed pump contribution of the generated SPDC state is shown in panels (a) and (b) at two propagation planes separated by 18 cm. The phase reconstructed via a modified GS algorithm is displayed in panel (c).

5. METHODS

A. Experimental Setup

The experimental setup is described in detail in Fig. 8. A 405 nm pump laser is generated as the second harmonic of a Ti:Sa pulsed laser (Chameleon Vision II). Then, a magnifying system of lenses with a pinhole in the beam's focus is used to generate the desired Gaussian beam that is then sent to the SLM. The beam's phase and amplitude are structured using the amplitude-phase masking technique [39], which requires appropriate phase masks displayed on the SLM and selecting the first diffraction order. The latter is achieved by placing an iris in a demagnifying system of lenses after the SLM. Sending the resulting structured pump beam through the BBO Type-I crystal, the SPDC is generated and collimated by a 75
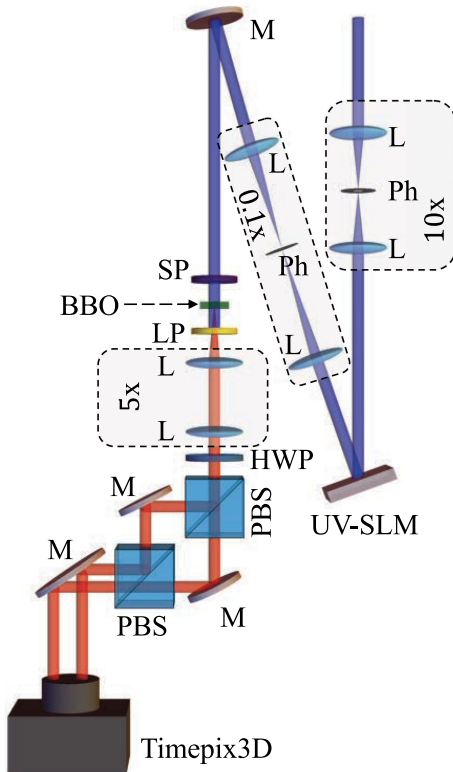
mm lens. After the crystal, the pump beam is filtered by a low-pass filter. Signal and idler photons are separated with 50% probability by a half wave-plate and a polarizing beamsplitter (PBS), instead of using a non-polarizing beamsplitter. This approach guarantees that the two photons are now orthogonally polarized. Using two mirrors and a PBS, one can simultaneously match the optical paths of the two photons and propagate them along parallel paths, with a relative displacement smaller than the camera sensor. A bandpass filter (centered at 810 nm and with 10 nm bandwidth) is mounted on the camera intensifier to select frequency degenerate photons. The Timepix camera collects spatially resolved time stamps with ~1 ns resolution [18] from which the 4D coincidence distribution is extracted.

B. Hypergeometric-Gaussian Modes

Hypergeometric-Gaussian modes $\mathrm{HyGG}_{p,\ell}$ with $p = -|\ell|$ are a set of paraxial modes whose expression in the waist plane is given by

$$\mathrm{HyGG}_{-|\ell|,\ell}(r, \phi, z = 0) \propto \exp(-r^2/w^2) \exp(i\ell\phi),$$

where (r, ϕ, z) are cylindrical coordinates, ℓ is an integer number, and w is a real parameter corresponding to the waist radius. Here, we consider the more general case where a quadratic phase is added on the waist plane:

$$\mathrm{HyGG}_{-|\ell|,\ell}(r, \phi, z = 0) \propto e^{-r^2/w^2} e^{-i\pi r^2/\lambda\mathcal{R}} e^{i\ell\phi}, \quad (12)$$

where $\mathcal{R}$ is the wavefront curvature radius. The expression for $\mathrm{HyGG}_{-|\ell|,\ell}(r, \phi, z)$ for arbitrary z can be obtained analytically by calculating the Fresnel propagator. It is convenient to use dimensionless coordinates: $\rho = r/w$, $\zeta = z/z_0$ (with $z_0 = \pi w^2/\lambda$), and $\xi = \mathcal{R}/z_0$. The Fresnel integral thus reads

$$\mathrm{HyGG}_{-|\ell|,\ell}(r, \phi, z) \propto \iint e^{-\rho'^2(1-i/\xi)} e^{i\ell\phi'}$$

$$\times e^{-i[\rho'^2+\rho^2-2\rho\rho'\cos(\phi-\phi')]/\zeta} \rho' d\rho' d\phi'$$

$$= e^{-i\left(\frac{\rho^2}{\zeta}-\ell\phi\right)}$$

$$\times \int_0^\infty \rho' d\rho' J_{|\ell|}\left(\frac{2\rho\rho'}{\zeta}\right) e^{-\left(\frac{\sigma+i}{\sigma}\right)\rho'^2},$$

$$(13)$$

Fig. 8. Detailed experimental setup. L, lens; Ph, pinhole; UV-SLM, ultraviolet spatial light modulator; M, mirror; SP, short-pass filter; LP, long-pass filter; HWP, half wave-plate; PBS, polarizing beamsplitter.

where $J_{|\ell|}(.)$ is a cylindrical Bessel function of order $|\ell|$ and $1/\sigma :=$ $1/\xi - 1/\zeta$. The solution to the last integral (see Ref. [40]) can be expressed in terms of modified Bessel functions:

$$\int_0^\infty \rho' d\rho' J_{|\ell|}(\alpha\rho') e^{-\beta\rho'^2}$$

$$= \frac{\sqrt{\pi}\alpha e^{-\frac{\alpha^2}{8\beta}}}{8\beta^{3/2}} \left[I_{\frac{|\ell|-1}{2}}\left(\frac{\alpha^2}{8\beta}\right) - I_{\frac{|\ell|+1}{2}}\left(\frac{\alpha^2}{8\beta}\right) \right], \qquad (14)$$

with $\alpha := 2\rho/\zeta$ and $\beta := \frac{\sigma+1}{\sigma} = 1 + i(1/\zeta - 1/\xi)$. The functions $I_{\frac{|\ell|\pm1}{2}}$ are modified Bessel functions of the first kind.

C. Details of Genetic Algorithm

Genetic algorithms evolve a population of candidate solutions toward optimal solutions to the problem of minimizing a cost function. In our case, the cost function is given by Eq. (11). The analytical expressions for the propagation of families of optical modes at a finite distance z, such as Hermite–Gauss or Laguerre–Gauss modes, enable the adoption of standard minimization routines. This is not possible in the case of aberrated beams, where there is no analytical formula for the propagated field. Genetic algorithms offer a suitable alternative, as these iterate from random guesses that evolve to the physical solutions of the optimization problem [41]. In the following, we detail the sequence of operators used in our genetic algorithm. An initial population of N individuals is randomly generated within the range $[-20, 20]$, where each individual is a set of real coefficients γ (genes) for the chosen Zernike polynomials. In groups of k, these individuals compete for the possibility to reproduce. Only the individual better minimizing the cost function within each pool is given access to the reproduction stage. This is the so-called *tournament* mechanism, working as a selection operator [42]. The reproduction occurs in the form of *blend crossover*, largely employed to mate real-valued individuals [43]. When two individuals reproduce, two newborns originate as a weighted mixture of the parents. To emulate the mutation of individuals in a natural environment, genetic mutations are included in the workflow as Gaussian noise with mean μ and standard deviation σ, potentially affecting each gene of newborn individuals [44]. Blend crossover and mutation are non-deterministic operators, occurring with probability p_c and p_m, respectively. To push the algorithm to a faster convergence, our algorithm is equipped with *elitism*, i.e., the best individual from the parent generation is guaranteed a place in the next one, replacing the worst individual of the offspring. The algorithm ends when a certain condition is verified [45]. In our implementation, the maximum number of generations N_{gen} is adopted as a termination criterion. The user defines by hand all the parameters determining the evolutionary sequence (also called *hyperparameters*). The complete set of hyperparameters used in our algorithm is listed in Table 1.

Table 1. Genetic Algorithm Hyperparameters

Population size	$N = 100$
Number of generations	$N_{\text{gen}} = 30$
Tournament size	$k = 4$
Crossover probability	$p_c = 0.9$
Mutation probability	$p_m = 0.04$
Gaussian mutation	$\mu = 0, \sigma = 0.5$

Disclosures. The authors declare no conflicts of interest.

Data availability. The data that support the findings of this study and the code used for the data analysis are available from the corresponding author upon reasonable request.

Supplemental document. See Supplement 1 for supporting content.

REFERENCES

1. D. F. V. James, P. G. Kwiat, W. J. Munro, *et al.*, "Measurement of qubits," Phys. Rev. A **64**, 052312 (2001).
2. G. M. D'Ariano, M. G. A. Paris, and M. F. Sacchi, "Quantum tomography," P. W. Hawkes, ed. *Advances in Imaging and Electron Physics*, (Elsevier, 2003), Vol. **128**, 206–309.
3. G. Torlai, G. Mazzola, J. Carrasquilla, *et al.*, "Neural-network quantum state tomography," Nat. Phys. **14**, 447–450 (2018).
4. M. Rambach, M. Qaryan, M. Kewming, *et al.*, "Robust and efficient high-dimensional quantum state tomography," Phys. Rev. Lett. **126**, 100402 (2021).
5. G. I. Struchalin, E. V. Kovlakov, S. S. Straupe, *et al.*, "Adaptive quantum tomography of high-dimensional bipartite systems," Phys. Rev. A **98**, 032330 (2018).
6. M. Agnew, J. Leach, M. McLaren, *et al.*, "Tomography of the quantum state of photons entangled in high dimensions," Phys. Rev. A **84**, 062101 (2011).
7. A. D'Errico, F. Hufnagel, F. Miatto, *et al.*, "Full-mode characterization of correlated photon pairs generated in spontaneous downconversion," Opt. Lett. **46**, 2388–2391 (2021).
8. A. C. Dada, J. Leach, G. S. Buller, *et al.*, "Experimental high-dimensional two-photon entanglement and violations of generalized Bell inequalities," Nat. Phys. **7**, 677–680 (2011).
9. M. Malik, M. Erhard, M. Huber, *et al.*, "Multi-photon entanglement in high dimensions," Nat. Photonics **10**, 248–252 (2016).
10. L. Chen, W. Zhang, Z. Wu, *et al.*, "Experimental ladder proof of Hardy's nonlocality for high-dimensional quantum systems," Phys. Rev. A **96**, 022115 (2017).
11. A. Cervera-Lierta, M. Krenn, A. Aspuru-Guzik, *et al.*, "Experimental high-dimensional Greenberger-Horne-Zeilinger entanglement with superconducting transmon qutrits," Phys. Rev. Appl **17**, 024062 (2022).
12. S. Watanabe, R. Matsumoto, and T. Uyematsu, "Tomography increases key rates of quantum-key-distribution protocols," Phys. Rev. A **78**, 042316 (2008).
13. F. Bouchard, F. Hufnagel, D. Koutný, *et al.*, "Quantum process tomography of a high-dimensional quantum communication channel," Quantum **3**, 138 (2019).
14. M. Genovese, "Real applications of quantum imaging," J. Opt. **18**, 073002 (2016).
15. D. Zia, N. Dehghan, A. D'Errico, *et al.*, "Interferometric imaging of amplitude and phase of spatial biphoton states," Nat. Photonics **17**, 1009–1016 (2023).
16. A. Nomerotski, "Imaging and time stamping of photons with nanosecond resolution in timepix based optical cameras," Nucl. Instrum. Methods Phys. Res., Sect. A **937**, 26–30 (2019).
17. K. Morimoto, A. Ardelean, M.-L. Wu, *et al.*, "Megapixel time-gated spad image sensor for 2d and 3d imaging applications," Optica **7**, 346–354 (2020).
18. A. Nomerotski, M. Chekhlov, D. Dolzhenko, *et al.*, "Intensified Tpx3Cam, a fast data-driven optical camera with nanosecond timing resolution for single photon detection in quantum applications," J. Instrum. **18**, C01023 (2023).
19. H. Defienne, B. Ndagano, A. Lyons, *et al.*, "Polarization entanglement-enabled quantum holography," Nat. Phys. **17**, 591–597 (2021).

20. Y. Zhang, D. England, A. Nomerotski, *et al.*, "High speed imaging of spectral-temporal correlations in Hong-Ou-Mandel interference," Opt. Express **29**, 28217–28227 (2021).

21. K. Morimoto, M.-L. Wu, A. Ardelean, *et al.*, "Superluminal motion-assisted four-dimensional light-in-flight imaging," Phys. Rev. X **11**, 011005 (2021).

22. Y. Zhang, A. Orth, D. England, *et al.*, "Ray tracing with quantum correlated photons to image a three-dimensional scene," Phys. Rev. A **105**, L011701 (2022).

23. B. Ndagano, H. Defienne, D. Branford, *et al.*, "Quantum microscopy based on Hong–Ou–Mandel interference," Nat. Photonics **16**, 384–389 (2022).

24. H. Defienne, P. Cameron, B. Ndagano, *et al.*, "Pixel super-resolution with spatially entangled photons," Nat. Commun. **13**, 3566 (2022).

25. G. S. Thekkadath, D. England, F. Bouchard, *et al.*, "Intensity interferometry for holography with quantum and classical light," Sci. Adv. **9**, eadh1439 (2023).

26. Z. G. Wang, M.-J. Sun, and D. Faccio, "From 3D to 5D: Computational light-in-flight imaging via an spad camera," Opt. Lasers Eng. **176**, 108088 (2024).

27. Y. Zhang, D. England, A. Orth, *et al.*, "Quantum light-field microscopy for volumetric imaging with extreme depth of field," Phys. Rev. Appl. **21**, 024029 (2024).

28. G. Ortolano, A. Paniate, P. Boucher, *et al.*, "Quantum enhanced non-interferometric quantitative phase imaging," Light Sci. Appl. **12**, 171 (2023).

29. S. P. Walborn, C. H. Monken, S. Pádua, *et al.*, "Spatial correlations in parametric down-conversion," Phys. Rep. **495**, 87–139 (2010).

30. F. M. Miatto, H. di Lorenzo Pires, S. M. Barnett, *et al.*, "Spatial Schmidt modes generated in parametric down-conversion," Eur. Phys. J. D **66**, 1–11 (2012).

31. V. Vidyapin, Y. Zhang, D. England, *et al.*, "Characterisation of a single photon event camera for quantum imaging," Sci. Rep. **13**, 1009 (2023).

32. R. W. Gerhberg and W. O. Saxton, "A practical algorithm for the determination of phase from image and diffraction plane picture," Optik **35**, 237–246 (1972).

33. J. R. Fienup, "Reconstruction of an object from the modulus of its Fourier transform," Opt. Lett. **3**, 27–29 (1978).

34. J. R. Fienup, "Phase retrieval algorithms: a comparison," Appl. Opt. **21**, 2758–2769 (1982).

35. S. P. Walborn, A. N. De Oliveira, S. Pádua, *et al.*, "Multimode Hong-Ou-Mandel interference," Phys. Rev. Lett. **90**, 143601 (2003).

36. A. E. Siegman, *Lasers* (University Science Books, 1986).

37. E. Karimi, G. Zito, B. Piccirillo, *et al.*, "Hypergeometric-Gaussian modes," Opt. Lett. **32**, 3053–3055 (2007).

38. M. Born and E. Wolf, *Principles of Optics: Electromagnetic Theory of Propagation, Interference and Diffraction of Light* (Elsevier, 2013).

39. E. Bolduc, N. Bent, E. Santamato, *et al.*, "Exact solution to simultaneous intensity and phase encryption with a single phase-only hologram," Opt. Lett. **38**, 3546–3549 (2013).

40. Y. L. Luke, *Integrals of Bessel Functions* (Courier, 2014).

41. J. H. Holland, *Adaptation in Natural and Artificial Systems: An Introductory Analysis with Applications to Biology, Control and Artificial Intelligence* (MIT, 1992).

42. D. E. Goldberg and K. A. Deb, "A comparative analysis of selectrion schemes used in genetic algorithms," Found. Genet. Algorithms **1**, 69–93 (1991).

43. L. J. Eshelman and J. D. Schaffer, "Real-coded genetic algorithms and interval-schemata," Found. Genet. Algorithms **2**, 187–202 (1993).

44. O. Kramer, *Genetic Algorithm Essentials* (Springer, 2017).

45. X. Yao, "An empirical study of genetic operators in genetic algorithms," Microprocess. Microprogramm. **38**, 707 (1993).